materials

MDPI

Article

Agile Inverse Design of Polarization-Independent Multi-Functional Reconfiguration Metamaterials Based on Doped VO_2

Bingyao Shan, Yang Shen, Xuran Yi, Xianqing Chi and Kejian Chen *

Shanghai Key Lab of Modern Optical System, Engineering Research Center of Optical Instrument and System, Ministry of Education, University of shanghai for Science and Technology, 516 Jungong Rd., Shanghai 200093, China

* Correspondence: ee.kjchen@gmail.com

Abstract: Increasing attention is being paid to the application potential of multi-functional reconfigurable metamaterials in intelligent communication, sensor networks, homeland security, and other fields. A polarization-independent multi-functional reconfigurable metasurface based on doped vanadium dioxide (VO_2) is proposed in this paper. It can be controlled to switch its function among three working modes: electromagnetically induced absorption (EIA), electromagnetically induced transparency (EIT), and asymmetrical absorption. In addition, deep learning tools have greatly accelerated the design of relevant devices. Such devices and the method proposed in this paper have important value in the field of intelligent reconfigurable metamaterials, communication, and sensing.

Keywords: metasurface; multi-functional; reconfiguration; electromagnetically induced absorption; vanadium dioxide; inverse design

check for updates

Citation: Shan, B.; Shen, Y.; Yi, X.; Chi, X.; Chen, K. Agile Inverse Design of Polarization-Independent Multi-Functional Reconfiguration Metamaterials Based on Doped VO_2. *Materials* **2024**, *17*, 3534. https://doi.org/10.3390/ma17143534

Academic Editor: Muamer Kadic

Received: 20 June 2024
Revised: 12 July 2024
Accepted: 15 July 2024
Published: 17 July 2024

Copyright: © 2024 by the authors. Licensee MDPI, Basel, Switzerland. This article is an open access article distributed under the terms and conditions of the Creative Commons Attribution (CC BY) license (https://creativecommons.org/licenses/by/4.0/).

1. Introduction

With the development of advanced communication technologies and the continued evolution of non-contact sensing and related fields, the demand for intelligent control of electromagnetic waves has become increasingly pressing. Metamaterials are smartly engineered structures with rationally designed structures and are composed of periodic subwavelength metal/dielectric structures that resonantly couple to the electric and/or magnetic components of the incident electromagnetic fields, exhibiting special properties. They have wide applicability in filtering [1–4], metalenses [5], negative refraction [6], EIT [7–9], EIA [10–12], nonreciprocal transmission [13], and sensing [14,15]. Typically, a metasurface exhibits a specific functionality upon fabrication, and enhancing their versatility through conventional approaches can result in substantial augmentation of complexity and manufacturing expenses. The functional diversity and switching convenience of devices can be realized by empowering them with the ability of functional reconfiguration and nonlinear response [16], for example, by incorporating active media, such as phase change material and liquid crystals, and by using thermal effects [17] and ultrafast nonlinear optical effects [18] on conventional metasurfaces [19]. Phase change materials have a wide range of applications in microfluidics, dynamic wave modulation [20,21], and sensing. Vanadium dioxide (VO_2) is a typical temperature-dependent phase change material. Sun et al. [22] proposed a reconfigurable broadband polarization conversion metasurface. Zhu et al. [23] designed a thermally controlled optical encryption metasurface using VO_2. Wang et al. [24] proposed a transmission/reflection mode switchable ultra-broadband metasurface filter. Undoped VO_2 exhibits a transition from an insulating dielectric state to a conducting metallic state at a critical temperature of approximately 67 °C (340 K) [25], while by doping tungsten ions in VO_2 [26], the critical temperature of the phase transition can be reduced by 21~28 °C/at. % to about 42 °C (315 K) [27]. Thereby, multi-functional

reconfigurable metasurface devices can be achieved by utilizing the VO_2 materials with different temperature-controlled phase change points in diverse structures.

In this paper, a multi-functional reconfigurable metasurface that achieves EIA, EIT, and asymmetrical absorption by using VO_2 materials in different structures is proposed. With the increasing complexity of devices, traditional structure-optimization methods are time-consuming and labor-intensive. To address this issue, we propose a deep learning-based inverse design method to accelerate the design optimization process and achieve favorable outcomes. The multi-functional reconfiguration metasurface and the related research methods proposed in this paper hold significant potential for applications in the design of intelligent metamaterials, as well as in communication and homeland security fields.

2. Structure Design and Simulation

The unit cell of the proposed multi-functional reconfigurable metasurface device is shown in Figure 1. Every part, from top to bottom, of the metasurface's structure was a gold cross structure with a VO_2 extender, gold C-type split-ring resonators (SRRs), and a gold I-type cross with extended structures of tungsten-ion-doped VO_2. The thickness of the polyimide films, from bottom to top, are h, h1, and h2, respectively. The structural parameters were optimized after inverse design using the DNN model and are as follows: h = 10 μm, h1 = 15 μm, h2 = 8 μm, P = 160 μm, w = 10 μm, l1 = 78 μm, t = 20 μm, I_e = 36 μm, d = 30 μm, g = 10 μm, r = 18 μm, l2 = 118 μm, C_e = 63 μm. The thickness of the gold used and VO_2 structures was set to 0.5 μm. The four C-type SRRs were placed in the four quadrants, respectively, and the angle to the adjacent axis was θ = 45°.

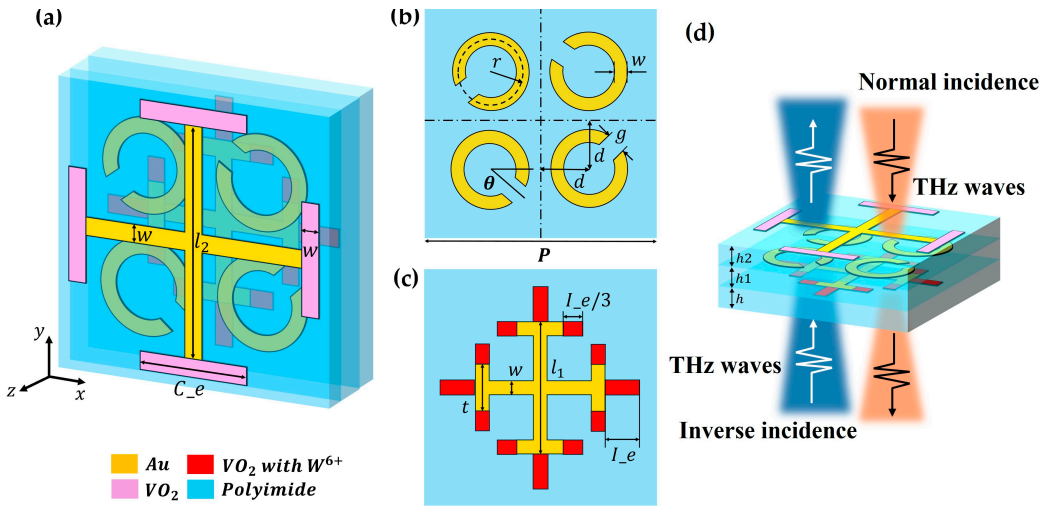

Figure 1. (**a**) The schematic of the proposed multi-functional reconfigurable metasurface unit. (**b**) The top view of the second layer (C-type SRRs). (**c**) The top view of the bottom layer (I-type cross and extend structures). (**d**) Side view of the device and two incidence directions.

The electromagnetic responses of the device are effectively investigated by CST Microwave Studio. Unit cell boundary conditions are applied in the x and y directions, while an open boundary is set in the z direction. Gold is modeled as a lossy metal, and its conductivity is 4.561×10^7 S/m [25]. The loss equation of polyimide films can be described as $\varepsilon_d = 3.5 + 0.009i$. The dielectric permittivity of VO_2 in the terahertz range can be characterized by the Drude model [28,29], expressed as $\varepsilon(\omega) = \varepsilon_\infty - \omega_p^2(\sigma_1)/(\omega^2 + i\gamma\omega)\Big)$, where ε_∞ is dielectric permittivity at the infinite frequency. Collision frequency γ is set to $\gamma = 5.75 \times 10^{13}$ rad/s, the plasma frequency ω_p, which depends on σ, can be approximated by $\omega_p^2(\sigma) = \frac{\sigma}{\sigma_0}\omega_p^2(\sigma_0)$, with $\sigma_0 = 3 \times 10^5$ S/m and $\omega_p(\sigma_0) = 1.4 \times 10^5$ rad/s [28]. In our simulation, both doped and undoped $\varepsilon_\infty = 12$. VO_2 is modeled as a material presenting a conductivity of 200 S/m in the insulating state, while in the metallic state, the conductivity is modeled as 2×10^5 S/m.

Since the device structure has rotational symmetry around the device axis, under normal incidence, it demonstrates the same absorption characteristics for different polarizations, as shown in Figure 2; therefore, the device has polarization-independent characteristics.

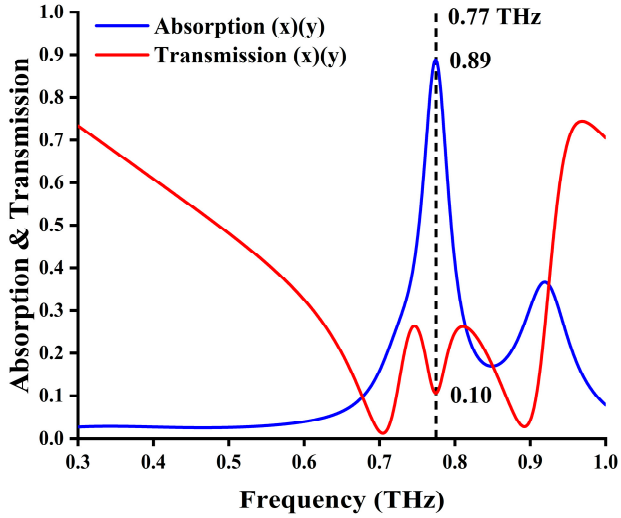

Figure 2. Absorption and transmission spectrum of the proposed multi-functional reconfigurable metasurface when the VO_2 is in its insulated state at room temperature. The device is optimized by inverse design network.

3. Results and Discussion

3.1. Working States of Device Changes with Temperature

3.1.1. (State 1)—EIA Phenomenon at Room Temperature

When the temperature is near room temperature (i.e., not exceeding 42 °C (315 K)), both doped and undoped VO_2 is in an insulated state (200 S/m for both). In this condition, the device exhibits significant electromagnetic wave absorption characteristics, as shown in Figure 2. The absorption rate A of the device can be calculated using $A(\omega) = 1 - R(\omega) - T(\omega) = 1 - |S_{11}|^2 - |S_{21}|^2$, where $R(\omega)$, $T(\omega)$, $S_{11}(\omega)$, and $S_{21}(\omega)$ are the reflectance, transmittance, reflection coefficient, and transmission coefficient, respectively. The reflectance and transmission for forward (inverse) incidence are $|S_{11}|^2\left(|S_{22}|^2\right)$ and $|S_{21}|^2\left(|S_{12}|^2\right)$, respectively. As shown in Figure 2, the absorption peak is mainly caused by the coupling of three metal structural layers (more details will be discussed later); it also produces a transmission valley at 0.77 THz, which can further confirm the generation of EIA phenomenon. Its operating frequency is like the frequency of the resonance reflection of the single-layer structure and the EIT phenomenon of the two-layer metamaterial.

3.1.2. (State 2)—Eit-like Phenomena When the W Ion-Doped VO_2 Turns to the Metallic State

When the temperature rises into the range from 42 °C (315 K) to 67 °C (340 K), the VO_2 doped with tungsten ions enters a metallic state while the undoped VO_2 remain in an insulated state. In this condition, the working frequency of the third-layer I-type cross resonator jumps to 0.50 THz, and only the first-layer cross is coupled with the second-layer SRR. The coupling results in an EIT-like phenomenon.

Figure 3a shows the results of the transmission calculation under normal incidence. At this time, the three-layer device is divided into two functional modules: firstly, the devices that can produce an EIT-like effect at 0.765 THz and are formed by the interaction between the cross on the top cross layer and the SRR on the second layer and, secondly, a single-frequency filter formed by an I-type cross of the third layer at 0.46 THz, as shown in Figure 3b,c. At 0.765 THz, the transmittance can reach 0.62, while the transmittance at 0.46 THz is as low as 0.07. Figure 3b,c provides the proof that the EIT-like effect is

mainly caused by the coupling of the top cross layer and the SRR layer. The EIT results are from a coherent cancellation between two different paths in a three-level atomic system. Through the EIT phenomenon, the transmission phenomenon can be generated in the same frequency of the initially non-transmitted structure.

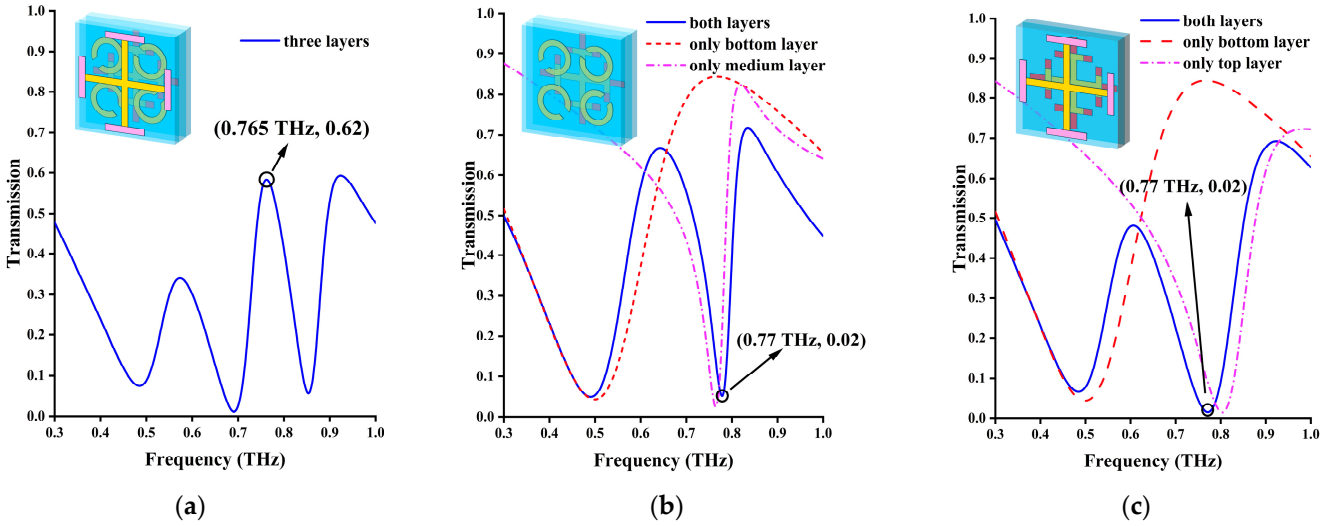

Figure 3. Doped VO_2 is in the metallic state at temperature range of 42~67 °C. (**a**) EIT-like phenomenon of three layers of metamaterials acting together. (**b**) Transmission spectrum of the second layer SRR and I-type of the third layer. (**c**) Transmission spectrum of the first layer cross and I-type of the third layer.

In this device, when the incident wave occurs with x polarization, the cross acts as the bright mode, and the C-shaped SRR acts as the dark mode. The opposite is true when the incident wave occurs with y polarization. The coherent cancellation between the cross and the SRR ring results in this transition from reflection and absorption to transmission at the frequency of 0.77 THz.

3.1.3. (State 3)—Asymmetrical Absorption at High Temperature

In our design, when the temperature of the device is above 67 °C (340 K), both VO_2 (undoped and doped) phases become metallic. As shown in Figure 4, changes in geometric parameters of the cross layer and the I-type cross layer due to VO_2 metallization and incident terahertz waves can be coupled to the metamaterial structures of the first and third layers at 0.45 THz and 0.50 THz, respectively, while the second layer still maintains a resonance frequency of 0.77 THz. When the cross of the first layer interacts with the I-type cross of the third layer, an asymmetric absorption effect is generated at 0.43 THz, with a lower absorption rate (0.14) from the cross side (normal incidence) and an absorption rate of 0.82 from the I-type cross side (reverse direction). This phenomenon of asymmetric absorption has a certain application prospect in electromagnetic isolation and stealth. Meanwhile, at 0.765 THz, due to the resonance reflection effect of SRR, the transmittance of both incidence directions is suppressed below 0.08, and the reflectance reaches 0.64 in normal incidence and 0.55 in the reverse incident direction. Other energy, which is induced by residual coupling (not fully decoupled) between SRR and the primary metal structure of the first and third layers, is absorbed. If complete decoupling can be achieved, then the perfect resonance reflection can be achieved at this frequency point, while the proposed structure temporarily cannot achieve complete decoupling.

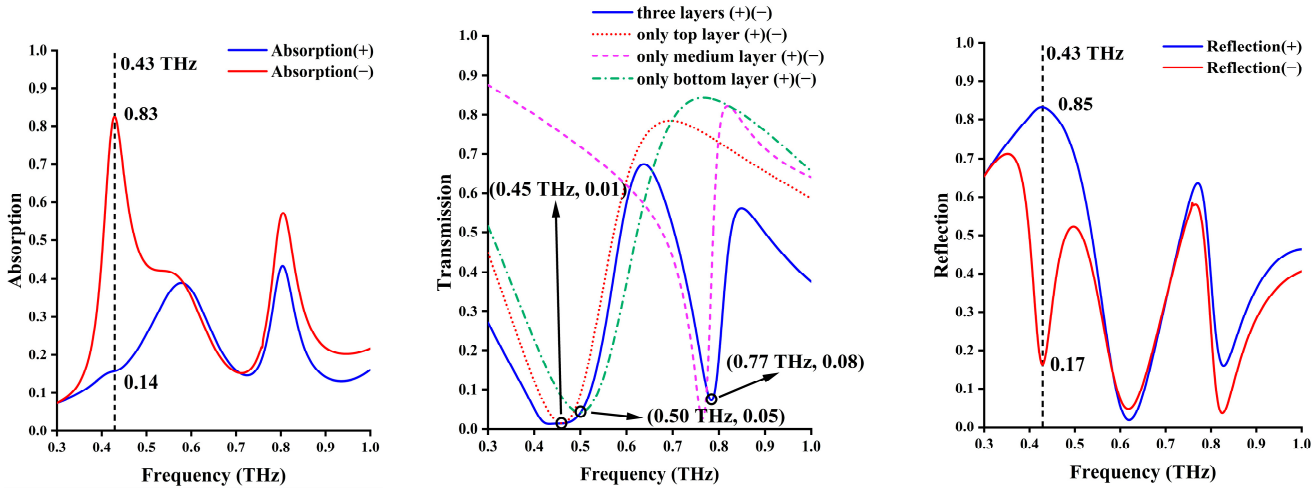

Figure 4. When both VO_2 phases change into metallic state above 67 °C. (**a**) Absorptivity; (**b**) transmittance; (**c**) reflectivity.

3.2. Discussion of the Working Mechanism and Other Related Issues

To better understand the phenomena and physical mechanisms that produce EIA phenomena at room temperature, the energy loss distribution of the proposed structure is analyzed, and the corresponding energy loss distribution when the incident wave in the x polarization direction is shown in Figure 5a. The electric and magnetic fields in the longitudinal section of the device are shown in Figure 5b,c. The EIA effect generated by this structure is mainly due to the vertical coupling between the three resonators. Due to the EIA effect, at 0.77 THz, most of the energy is lost through the SRR and the I-type cross, and a small part of the energy is lost through the cross-layer. The cross will generate strong loss points at the upper and lower two endpoints; the mechanism of the I-type cross is similar to the cross. The energy gathered in the metal will be lost in the VO_2 and on the surface of the PI film due to the characteristics of the magnetic loss material without phase transition. The SRR ring shows a diagonal activation state due to the x polarization incident, and the energy is mainly lost at the gap between the SRRs and the PI dielectric material of the first and second layers.

When the temperature rises into the range of 42 °C (315 K) to 67 °C (340 K), the bottom VO_2 undergoes a phase change, and an EIT-like phenomenon occurs between the first and second layers. In order to better understand the physical properties of this EIT behavior, the surface current distribution in Figure 6 is calculated at the frequencies of two transmission troughs and one transmission peak, when the polarization direction of the incident wave is x polarization. Since the operating frequency of the bottom layer is moved to 0.43 THz under the phase-change action of doped VO_2, the interaction of the three-layer structure at 0.77 THz becomes only a strong interaction between the first and second layers. Under the action of the external incident polarized wave, the bar parallel to the incident electric field is excited. Due to the interaction between the first and second layers, strong coupled resonance is excited on the second and fourth quadrant SRRs of the second layer (which cannot be directly strongly excited by the external × polarization incidence). As a result of the strong interaction between the first layer bar and the second SRR, electromagnetic-induced transmission occurs. Although the first and second layers also interact at frequencies of 0.70 THz and 0.855 THz, the current of the second-layer SRR induced by it is either very weak (such as 0.70 THz) or has a phase difference with the surface current of the first layer (opposite direction, @ 0.855 THz); thus, EIT cannot be achieved in these places. From the observed electric field distributions on the surfaces, it can

be determined that the strong interaction between the cross of the first layer and the gold SRR of the second layer is the main reason for the electromagnetically induced transparency.

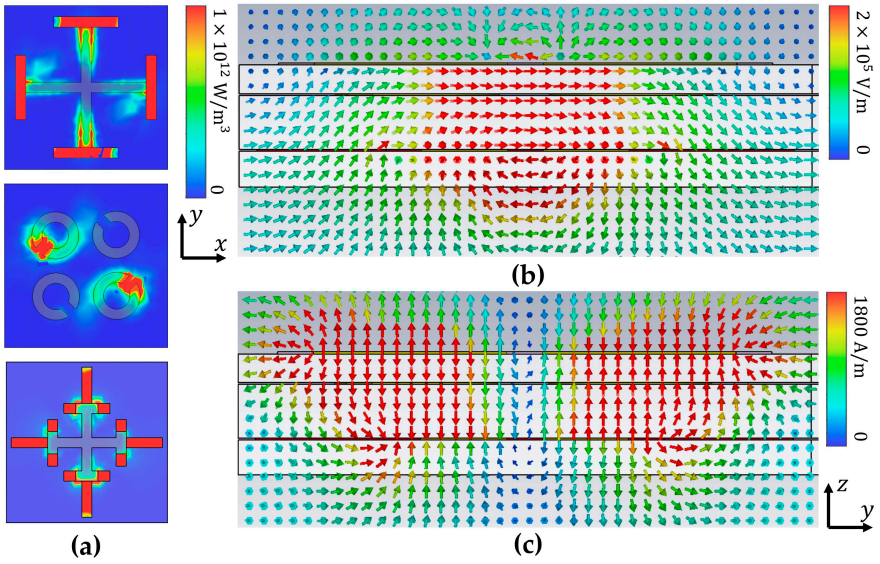

Figure 5. Simulation results of (**a**) power loss, (**b**) electric fields, and (**c**) magnetic fields at 0.77 THz, when they are at room temperature.

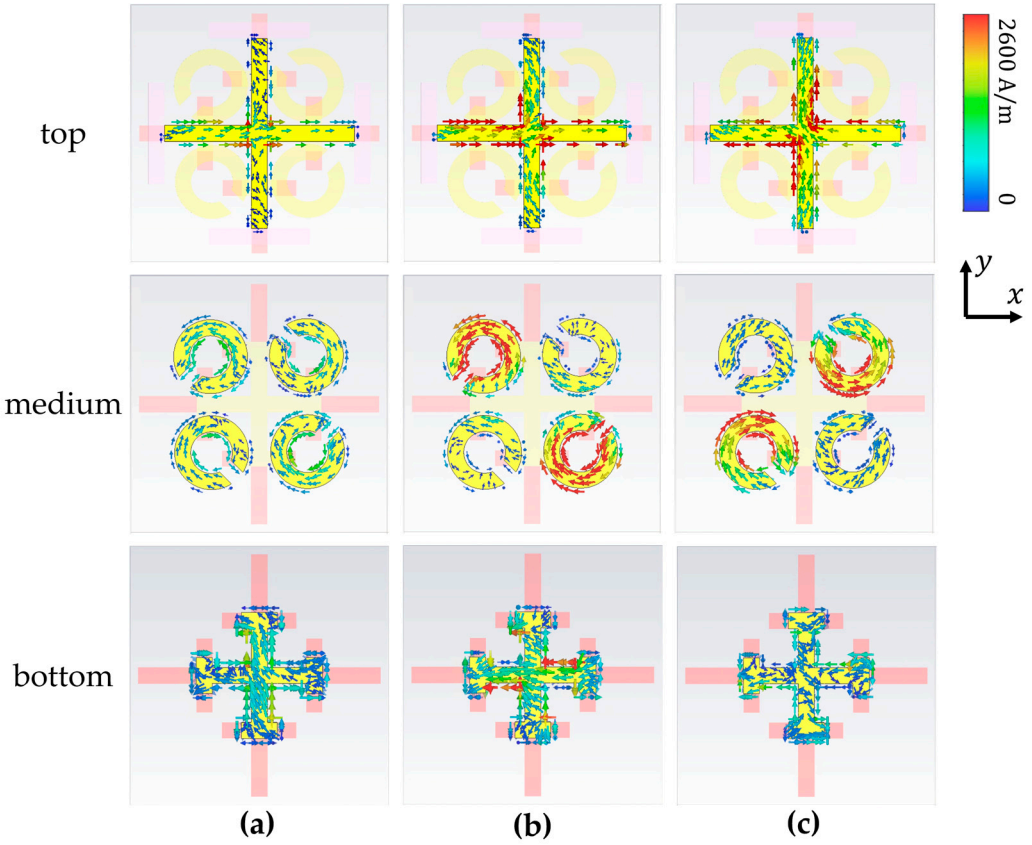

Figure 6. Surface current distribution of the three-layer structure at frequencies of 0.70 THz (**a**), 0.765 THz (**b**), and 0.855 THz (**c**) at the range of 42 °C (315 K) to 67 °C (340 K).

When the temperature rises to above 67 °C (340 K), both doped VO_2 and undoped VO_2 become metallic. At this time, asymmetric absorption can be observed at 0.43 THz. The absorption is weak at forward incidence and very strong at reverse incidence. The

absorption is mainly formed by the coupling of the first layer of the cross and the bottom layer of the I-shaped crosses with their VO_2-extended structures. The operating frequency of the second layer of the SRR ring is fixed at 0.77 THz, so it has no effect on the absorption of this frequency. As shown in Figure 7a, at forward incidence, the current of the three-layer structure is small and has little effect on the incident wave. In Figure 7b, the strong absorption at reverse incidence is caused by the antiparallel current between the top cross and the bottom VO_2 film. This current loop generates an artificial magnetic dipole moment which will interact strongly with the incident magnetic field and contribute to the absorption.

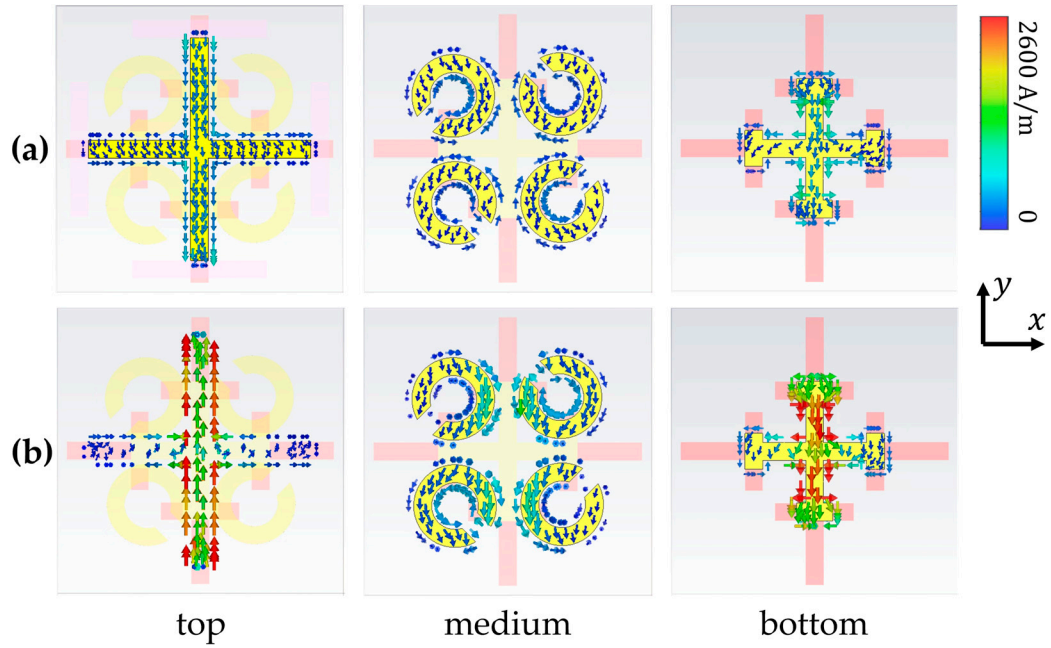

Figure 7. Surface current of the three-layer structure at 0.43 THz. (**a**) Forward incidence and (**b**) reverse incidence when temperature is above 67 °C (340 K).

3.3. Potential Fabrication Process of the Proposed Structure

In practical applications, conventional microelectronic semiconductor process-related procedures can be considered for the fabrication of devices. These procedures include standard ultraviolet lithography [30] with thin-film deposition techniques [31]. The possible manufacturing process can start with a 10 μm PI film, as shown in Figure 8. The following instructions would need to be carried followed: (a) spin-coat photoresist and perform photolithography; (b) deposit a 0.5 μm thick metal layer on the PI film using magnetron sputtering or electron beam evaporation; (c) dissolve the photoresist, leave the gold pattern, spin-coat the photoresist again, and perform overlay process for photolithography; (d) magnetron sputter a 0.5 μm thick doped VO_2 layer; (e) dissolve the photoresist and cover with a 15 μm thick polyimide layer; (f) spin-coat photoresist, perform photolithography, and then deposit the metal layer; (g) dissolve the photoresist and cover with an 8 μm thick polyimide layer again; (h) spin-coat photoresist, perform optical lithography, and deposit a 0.5 μm thick metal layer by electron beam evaporation; (i) after dissolving the photoresist, spin-coat the photoresist again, perform photolithography and magnetron sputtering of a 0.5 μm thick VO_2 layer, and anneal the remaining VO_2; (j) dissolve the photoresist to complete the device fabrication. Then, a THz-TDS system can be used for spectrum measurement. As the focus of this paper is to explore the application value of deep learning in the field of convenient reverse design of multifunctional reconfigurable metamaterials, those seeking more details regarding the possible fabrication and measurement method can refer to the papers mentioned above.

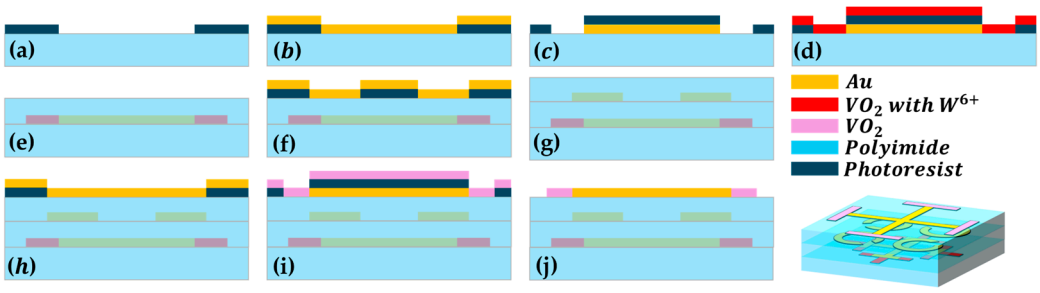

Figure 8. Potential fabrication process of the processed structure. (**a**) photolithography; (**b**) metal deposition; (**c**) liftoff and overlay photolithography; (**d**) doped-VO_2 deposition; (**e**) liftoff and covered with polyimide layer; (**f**) the process for the second metal layer; (**g**) liftoff, and cover polyimide layer; (**h**) the process for the third metal layer; (**i**) liftoff, and deposit VO_2 layer; (**j**) liftoff, and complete the device fabrication.

From the simulation results in Figure 9, it can be concluded that if the misplacement between the metasurface structure layers is within 3 μm, the spectrum of the devices will mostly have a slight blue shift, and a minor red shift may occur when the first layer shifts towards the y direction and the second layer shifts in the x direction. Because the precision of the photolithography-related technology is much better than that of 3 μm, the fabrication of the proposed device is realizable, although the process complexity may be relatively high.

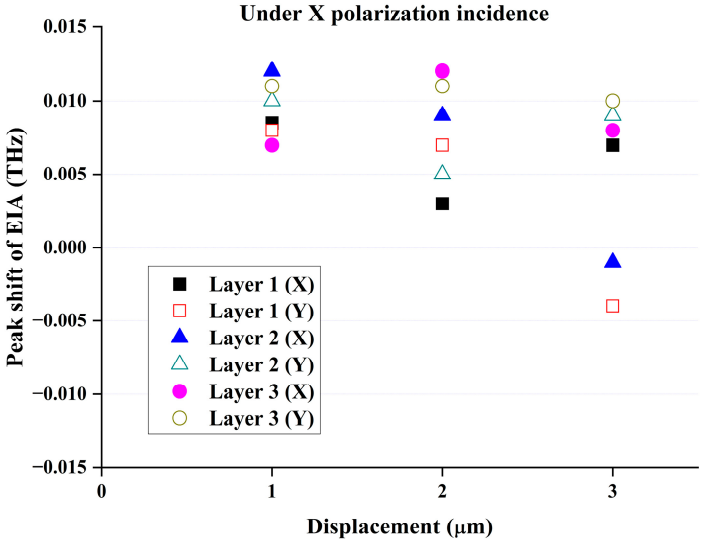

Figure 9. The effect of the displacement of metasurface layers (simulation results).

3.4. Inverse Design Optimization Based on Deep Neural Network (DNN)

Machine learning (ML) offers a promising solution that can generate results with limited computing resources and reduce time-consuming computing processes [32]. The design process includes two steps: forward design and reverse design (see Figure 10). This paper selects a deep neural network (DNN) as the deep learning model. A DNN usually contains multiple hidden layers, which provide enough hidden units to represent complex functions according to the universal approximation theorem [33]. Therefore, it is possible to reveal the hidden relationship between variables. To train a DNN, several parameters of electromagnetic spectra and metasurfaces were defined as data sets. Because deep learning is used for the agile design of the device, the absorption spectrum in the x polarization direction of the polarization-independent metamaterial structures is used for data collection and model training. During the data collection process, structural parameters were generated randomly to reduce the difficulty of training. Five structural

parameters that have a significant impact on the spectral response (for example, EIA) were selected for data collection. The parameters and their ranges are shown in Table 1.

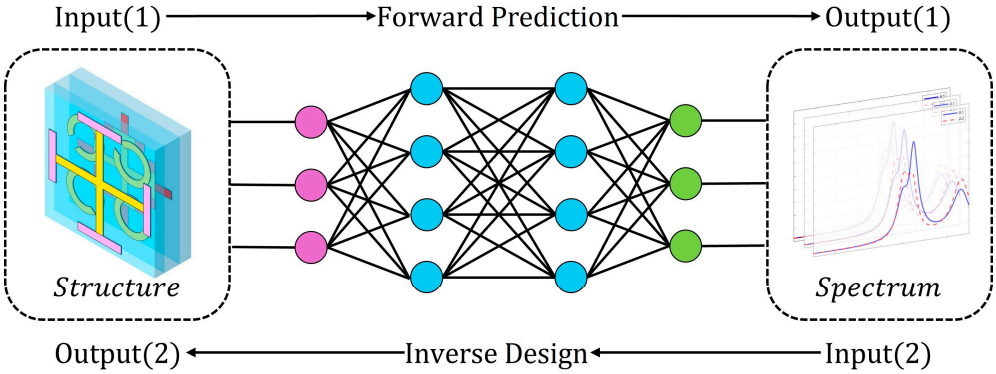

Figure 10. Flow chart of forward prediction and inverse design using DNN.

Table 1. Scanning parameters.

Parameters	*l*1	*t*	*l*2	*r*	*d*
Min size (μm)	74	17	113	17	8
Max size (μm)	84	22	123	20	12
Samples	6	6	6	4	3

The parameter table generated was saved into a file, and the spectral line data in the front and rear incident directions of the device were collected using Matlab-CST joint simulation. A total of 2592 sets of valid data were simulated. Then, the entire data set was divided as follows: 80% into a training set and 20% into a test set.

Here, we use the EIA state of three-layer coupling as an example to illustrate how to inverse design a more complex multi-function metamaterial device. The data set collected from the previous simulation was entered into the model for training. After 2000 iterations, when the test loss of the test set drops to 4.7, the training process converges, and the loss becomes stable. The loss curve of the test set is shown in Figure 11a. Once the inverse learning model is trained, we can predict the desired structural parameters through the generator in a few milliseconds.

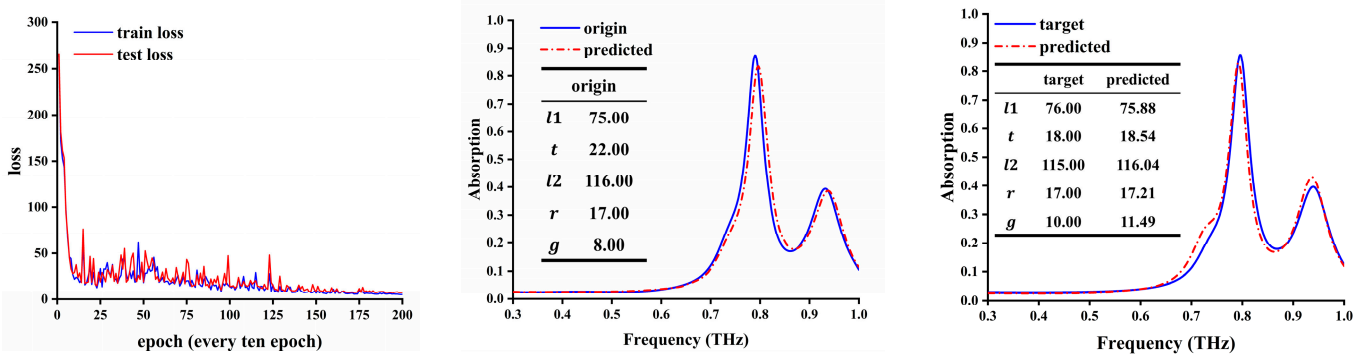

(**a**) (**b**) (**c**)

Figure 11. (**a**) The loss curve of training and test. (**b**) Forward design and (**c**) inverse design of target and predicted spectrum of structures.

To further verify the validity of model-based prediction parameters, spectra were predicted by the forward network (Figure 11b). The predicted device structure parameters generated by the inverse network were rounded and simulated again in CST 2022 software, and the predicted spectra were compared with the target spectra (Figure 11c). The blue

solid line is the target simulation curve, and the red dashed line is the simulation result of the DNN predicting structural parameters.

It can be seen from the results that the spectra obtained by our prediction model can accurately describe the EIA effect generated by the three-layer structure, and the results also show that a DNN has good learning ability and adaptability and can be extended to the design of new metasurfaces.

To achieve better EIA effect, we manually generated a spectrum with ideal absorption at two target frequencies (0.77 THz and 0.83 THz) and input them into the DNN model for inverse design and prediction of parameters. Then, we used CST software to simulate and verify it again. The obtained simulation results with the prediction of parameters are shown in Figure 12a,b with the ideal spectrum. The analysis shows that after using the DNN model for inverse design, the three-layer structure can be designed and optimized quickly and accurately. Due to the imperfection of the current model, the result may not be the optimal state of the structure. We can manually fine-tune the model parameters to achieve the best state based on the model parameters generated by the DNN model. By using inverse learning, the design time of complex devices can be greatly shortened to about 1/1000 to 1/10,000 of the original time.

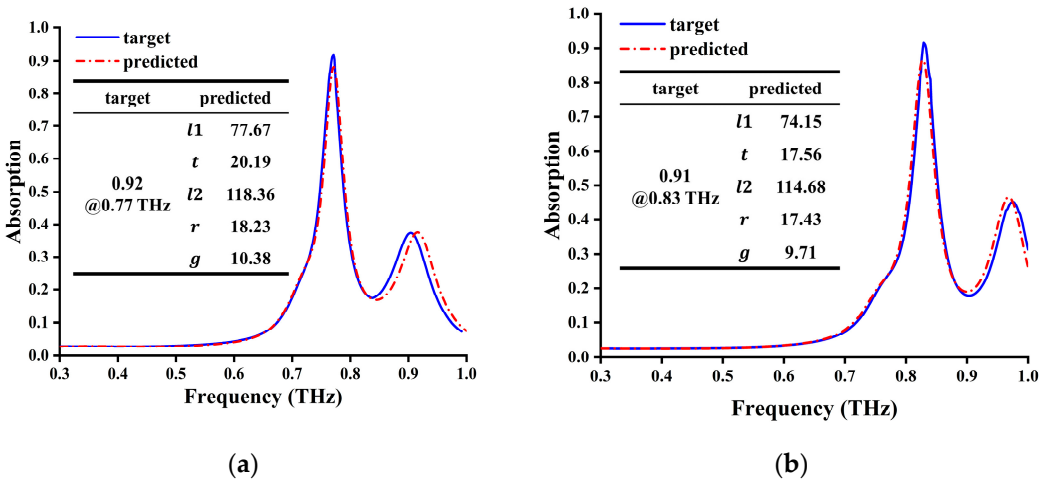

Figure 12. The ideal EIA spectrum and simulation result at (**a**) 0.77 THz and (**b**) 0.83THz.

4. Summary

A polarization-independent multi-functional reconfigurable metasurface is proposed. At room temperature, the proposed metasurface device exhibits the characteristics of EIA at 0.77 THz, and the absorption rate can reach 0.89 (Q factor is 14.81). When the doped VO_2 is in the metallic state at a temperature range of 42~67 °C, the interaction between the top cross layer and the SRR layer results in an EIT-like phenomenon at 0.77 THz (its Q factor is 8.47), when the narrow-band filter at 0.5 THz. When the temperature keeps increasing and both VO_2 (doped and undoped) are in the metallic state, asymmetrical absorption can be achieved at 0.43 THz, and the absorption rate can reach 0.82 (its Q factor is only 3.69, due to a flat stage); the absorption rate difference can reach 0.68. If needed, metasurface devices with higher Q value can be obtained by adopting some quasi-BIC resonance structures into the design (for example, asymmetric SRRs [3,4]), but the polarization-independent properties may be sacrificed. By leveraging the phase transition property of VO_2, the proposed metamaterials can reconfigure the functionality of VO_2 without altering its geometric shape. Simultaneously, the design optimization process was accelerated with a DNN and the inverse learning method to expedite the design optimization process. Consequently, VO_2 can potentially revolutionize the development of optical switchable components, enabling multifunctionality within a single device, and the optimization method based on deep learning holds significant application value and broad prospects in intelligent metamaterial design, communication, and other related fields.

Author Contributions: Conceptualization, B.S. and K.C.; methodology, B.S., X.Y. and Y.S.; formal analysis, B.S.; investigation, B.S., X.C. and Y.S.; data curation, B.S.; writing—original draft preparation, B.S.; writing—review and editing, K.C., Y.S., X.Y. and X.C.; visualization, B.S.; supervision, K.C. All authors have read and agreed to the published version of the manuscript.

Funding: This research was funded by National Natural Science Foundation of China, grant number 61205095; Shanghai Young College Teacher Develop funding schemes, grant number slg11006; and, in part, by Shanghai College Student Innovation and Entrepreneurship Training Program, grant number SH2024062.

Data Availability Statement: The original contributions presented in the study are included in the article, further inquiries can be directed to the corresponding author.

Acknowledgments: We gratefully acknowledge L. Liu from BUPT for the fruitful discussion on reverse design using DNN neural networks.

Conflicts of Interest: The authors declare no conflicts of interest.

References

1. Chen, Y.; Chen, K.; Zhang, D.; Li, S.; Xu, Y.; Wang, X.; Zhuang, S. Ultrabroadband microwave absorber based on 3D water microchannels. *Photon. Res.* **2021**, *9*, 1391–1396. [CrossRef]
2. Abujetas, D.R.; Barreda, Á.; Moreno, F.; Litman, A.; Geffrin, J.-M.; Sánchez-Gil, J.A. High-Q Transparency Band in All-Dielectric Metasurfaces Induced by a Quasi Bound State in the Continuum. *Laser Photonics Rev.* **2020**, *15*, 2000263. [CrossRef]
3. Li, J.; Li, J.; Zheng, C.; Yue, Z.; Wang, S.; Li, M.; Zhao, H.; Zhang, Y.; Yao, J. Free switch between bound states in the continuum (BIC) and quasi-BIC supported by graphene-metal terahertz metasurfaces. *Carbon* **2021**, *182*, 506–515. [CrossRef]
4. Liu, Y.; Zhang, Q.; Xing, X.; Zou, D.; Mao, B.; Yao, J.; Ouyang, C.; Wang, Z.; Wu, L. Terahertz narrowband filter metasurfaces based on bound states in the continuum. *Opt. Express* **2023**, *31*, 35272–35281. [CrossRef]
5. Chen, Z.N.; Li, T.; Qing, X.; Shi, J.; Li, S.; Su, Y.; Liu, W.E.I.; Xue, C.; Lou, Q.; Jiang, Z.H.; et al. Microwave Metalens Antennas. *Proc. IEEE* **2023**, *111*, 978–1010. [CrossRef]
6. Yang, Y.; Ge, Y.; Li, R.; Lin, X.; Jia, D.; Guan, Y.; Yuan, S.; Sun, H.; Chong, Y.; Zhang, B. Demonstration of negative refraction induced by synthetic gauge fields. *Sci. Adv.* **2021**, *7*, eabj2062. [CrossRef] [PubMed]
7. Shi, H.; Yan, S.; Yang, X.; Wu, X.; Wu, W.; Hua, E. A Nanosensor Based on a Metal-Insulator-Metal Bus Waveguide with a Stub Coupled with a Racetrack Ring Resonator. *Micromachines* **2021**, *12*, 495. [CrossRef] [PubMed]
8. Le, T.-T. Electromagnetically Induced Transparency (EIT) Like Transmission Based on 3 × 3 Cascaded Multimode Interference Resonators. *Micromachines* **2018**, *9*, 417. [CrossRef] [PubMed]
9. Liu, Z.; Qi, L.; Shah, S.M.A.; Sun, D.; Li, B. Design of Broad Stopband Filters Based on Multilayer Electromagnetically Induced Transparency Metamaterial Structures. *Materials* **2019**, *12*, 841. [CrossRef]
10. Caillas, A.; Suffit, S.; Filloux, P.; Lhuillier, E.; Degiron, A. Anomalous Absorption in Arrays of Metallic Nanoparticles: A Powerful Tool for Quantum Dot Optoelectronics. *Nano Lett.* **2022**, *22*, 2155–2160. [CrossRef]
11. Wan, B.-F.; Li, B.-X.; Zhang, H.-F. Theoretical Study of Dual-Function Sensor for Analysis of Blood Composition and Glucose Concentration Based on Nonreciprocal Analog of the Electromagnetically Induced Absorption. *IEEE Trans. Instrum. Meas.* **2023**, *72*, 7007610. [CrossRef]
12. Zeng, L.; Li, B.-X.; Zhang, H.-F. Nonreciprocal Electromagnetically Induced Unidirectional Absorption Based on the Quasi-Periodic Metastructure and Its Application for Permittivity Sensing. *IEEE Trans. Instrum. Meas.* **2023**, *72*, 6001412. [CrossRef]
13. Lawrence, M.; Barton, D.R., III; Dionne, J.A. Nonreciprocal Flat Optics with Silicon Metasurfaces. *Nano Lett.* **2018**, *18*, 1104–1109. [CrossRef]
14. Sun, W.; Liang, Z.; Shi, X.; Yang, F.; Dong, Y.; Dai, R.; Jia, Y.; Xin, W.; Hou, E.; Wu, Z. Potential of high Q dual band Mid-Infrared metasurfaces with Quasi-BIC for refractive index sensing. *Opt. Laser Technol.* **2024**, *174*, 110631. [CrossRef]
15. Karawdeniya, B.I.; Damry, A.M.; Murugappan, K.; Manjunath, S.; Bandara, Y.M.N.D.Y.; Jackson, C.J.; Tricoli, A.; Neshev, D. Surface Functionalization and Texturing of Optical Metasurfaces for Sensing Applications. *Chem. Rev.* **2022**, *122*, 14990–15030. [CrossRef] [PubMed]
16. Carletti, L.; Gandolfi, M.; Rocco, D.; Tognazzi, A.; de Ceglia, D.; Vincenti, M.A.; De Angelis, C. Reconfigurable nonlinear response of dielectric and semiconductor metasurfaces. *Nanophotonics* **2021**, *10*, 4209–4221. [CrossRef]
17. Kats, M.A.; Blanchard, R.; Genevet, P.; Yang, Z.; Qazilbash, M.M.; Basov, D.N.; Ramanathan, S.; Capasso, F. Thermal tuning of mid-infrared plasmonic antenna arrays using a phase change material. *Opt. Lett.* **2013**, *38*, 368–370. [CrossRef] [PubMed]
18. Ning, T.; Li, X.; Zhang, Z.; Huo, Y.; Yue, Q.; Zhao, L.; Gao, Y. Ultimate conversion efficiency of second harmonic generation in all-dielectric resonators of quasi-BICs in consideration of nonlinear refraction of dielectrics. *Opt. Express* **2021**, *29*, 17286. [CrossRef]
19. He, Q.; Sun, S.; Zhou, L. Tunable/Reconfigurable Metasurfaces: Physics and Applications. *Research* **2019**, *2019*, 1849272. [CrossRef] [PubMed]

20. Shadrivov, I.V.; Kapitanova, P.V.; Maslovski, S.I.; Kivshar, Y.S. Metamaterials controlled with light. *Phys. Rev. Lett.* **2012**, *109*, 083902. [CrossRef]
21. Liu, M.; Wei, R.; Taplin, J.; Zhang, W. Terahertz Metasurfaces Exploiting the Phase Transition of Vanadium Dioxide. *Materials* **2023**, *16*, 7106. [CrossRef] [PubMed]
22. Sun, X.; Qu, Z.; Yuan, J.; Wang, Q. Reconfigurable broadband polarisation conversion metasurface based on VO_2. *Photonics Nanostructures Fundam. Appl.* **2022**, *50*, 101012. [CrossRef]
23. Zhu, S.; Dong, B.; Guo, G.; Lu, X.; Xu, Q.; Han, J.; Huang, W.; Ma, H.; Wang, Y.; Zhang, X.; et al. Terahertz Metasurfaces for Thermally Controlled Optical Encryption. *Laser Photonics Rev.* **2023**, *17*, 2300233. [CrossRef]
24. Wang, D.; Cai, B.; Yang, L.; Wu, L.; Cheng, Y.; Chen, F.; Luo, H.; Li, X. Transmission/reflection mode switchable ultra-broadband terahertz vanadium dioxide (VO_2) metasurface filter for electromagnetic shielding application. *Surf. Interfaces* **2024**, *49*, 104403. [CrossRef]
25. Song, Z.; Chen, A.; Zhang, J.; Wang, J. Integrated metamaterial with Functionalities of absorption and electromagnetically induced transparency. *Opt. Express* **2019**, *27*, 25196–25204. [CrossRef] [PubMed]
26. Tien, C.-L.; Chiang, C.-Y.; Wang, C.-C.; Lin, S.-C. Optical, Electrical, Structural, and Thermo-Mechanical Properties of Undoped and Tungsten-Doped Vanadium Dioxide Thin Films. *Materials* **2024**, *17*, 2382. [CrossRef] [PubMed]
27. Morin, F.J. Oxides which show a metal-to-insulator transition at the neel temperature. *Phys. Rev. Lett.* **1959**, *3*, 34–36. [CrossRef]
28. Wang, S.; Cai, C.; You, M.; Liu, F.; Wu, M.; Li, S.; Bao, H.; Kang, L.; Werner, D.H. Vanadium dioxide based broadband THz metamaterial absorbers with high tunability: Simulation study. *Opt. Express* **2019**, *27*, 19436–19447. [CrossRef] [PubMed]
29. Song, Z.; Deng, Y.; Zhou, Y.; Liu, Z. Terahertz toroidal metamaterial with tunable properties. *Opt. Express* **2019**, *27*, 5792–5797. [CrossRef]
30. Zhu, D.; Liu, Z.; Raju, L.; Kim, A.S.; Cai, W. Building Multifunctional Metasystems via Algorithmic Construction. *ACS Nano* **2021**, *15*, 2318–2326. [CrossRef]
31. Su, J.L.; You, J.W.; Chen, L.; Yu, X.Y.; Yin, Q.C.; Yuan, G.H.; Huang, S.Q.; Ma, Q.; Zhang, J.N.; Cui, T.J. MetaPhyNet: Intelligent design of large-scale metasurfaces based on physics-driven neural network. *J. Phys. Photonics* **2024**, *6*, 035010. [CrossRef]
32. Fu, C.F.; Zhang, L.; Liu, L.J.; Dong, S.H.; Yu, W.J.; Han, L.F. RCS reduction on patterned graphenebased transparent flexible metasurface absorber. *IEEE Trans. Antennas Propag.* **2023**, *71*, 2005–2010. [CrossRef]
33. Jia, Y.; Wang, G.; Jiang, J.J.; Miao, F.J.; Shao, Y.B.; Gao, Y.C. Multi-functional dual-band polarization converter based on graphene and vanadium dioxide metasurfaces. *Diam. Relat. Mat.* **2023**, *135*, 109881. [CrossRef]

Disclaimer/Publisher's Note: The statements, opinions and data contained in all publications are solely those of the individual author(s) and contributor(s) and not of MDPI and/or the editor(s). MDPI and/or the editor(s) disclaim responsibility for any injury to people or property resulting from any ideas, methods, instructions or products referred to in the content.